FDMP, vol.1, no.1, pp.45-62, 2005

Numerical Simulation of CZ Crystal Growth of Oxide

T. Tsukada[1], M. Kobayashi[2], C. J. Jing[3] and N. Imaishi[4]

Abstract: In this paper, our recent numerical studies on the Czochralski (CZ) crystal growth of oxide are surveyed. In the first part of the analysis, a "global" heat transfer model for an inductively heated CZ furnace is introduced and depicted in detail. It is emphasized that accounting for the internal radiation within the crystal and/or melt is of crucial importance since they are often semitransparent to infrared radiation. Results coming from such a "global" approach suggest that the melt/crystal interface shape is strongly affected by the optical properties of the crystal, of the melt and by the melt convection. The second part of the article is devoted to illustrate some convective instabilities that can arise in the CZ oxide melt. They are discussed within the framework of a numerical analysis for unsteady, three-dimensional flows. It is demonstrated that "spoke patterns" seen on the melt surface are due to a Marangoni instability, while "wave patterns" are caused by a baroclinic instability.

keyword: CZ crystal growth, Oxide, Numerical simulation, Internal radiation, Marangoni instability, Baroclinic instability.

1 Introduction

Oxide single crystals such as yttrium aluminum garnet, gadolinium gallium garnet and lithium niobate are utilized as solid-state laser hosts and materials for acoust-opt-electronic devices, and are commonly grown by the Czochralski (CZ) method which is one of the crystal growth techniques from the melt. Melt flow and other transport phenomena in the CZ furnace are strongly influenced by forces, such as buoyancy, the centrifugal and Coriolis forces due to the crystal rotation, and the thermocapillary force due to the temperature dependence of the surface tension on the melt surface. Their intensity and interaction determine the melt flow structure, the heat and mass (dopant) transport in the furnace, the melt/crystal interface shape, and consequently the quality of the final oxide crystals. For instance, gaseous bubble inclusions, the appearance of the central column-shaped core area, defect and crack formations in the crystal (all factors closely related to the crystal quality) are influenced by the melt flow patterns and temperature distributions in the crystal and melt and additionally by the melt/crystal interface shape. Moreover, in addition to the convective effects, the crystals tend to be sometimes twisted or separated from the melt surface during growth process, depending on the shape of the melt/crystal interface.

Although the CZ furnace has a very simple structure, the heat transfer mechanism is very complex. Since most of the oxide melt growth is operated at very high temperature, the heat transfer is controlled by radiation as well as conduction and convection. Particularly, when oxide single crystals are not opaque to infrared radiation, the radiative heat absorption and emission in the crystal strongly influence the heat transfer behavior and the shape of the melt/crystal interface. For instance, it is experimentally known that the radiative heat transfer through the crystal renders the interface deeply convex toward the melt [Cockayne, Chesswas and Gasson (1969); Kvapil, Kvapil, Manek, Perner, Autrata and Scuer (1981)], and that the change in the absorption coefficient of the crystal affects the growth characteristics [Brandle, Fratello, Valentine and Stokowski (1987); Okano, Tsuji, Yoon, Hoshikawa and Fukuda (1994)]. Therefore, it is important to acquire correct knowledge on transport phenomena in the furnace, in order to grow large, high-quality oxide single crystals. Also, the heat transfer and the interface shape must be properly controlled.

Recently, numerical simulations have been extensively used as an useful method to investigate these effects. In order to calculate the temperature distributions in the

---

[1] Osaka Prefecture University, Sakai, Japan
[2] Hachinohe Institute of Technology, Hachinohe, Japan
[3] Southwest Jiaotong University, Sichuan, P. R. of China
[4] Kyushu University, Kasuga, Japan

melt and crystal, some parameters/conditions must be known: geometrical conditions, such as the size of the crucible, diameter and length of the crystal, operating conditions, such as, rotation rate of the crystal, volume of the melt, temperature of the crucible and ambient solid walls and also thermophysical properties of the materials. In addition to those values, the shape of the melt/crystal interface, the heater power or the pulling rate should be also known. These conditions can not be given *a priori*, however, since the heat transfer mechanisms in a CZ furnace are tightly combined each other often in non-linear ways.

In practice, all these combined values/conditions can be determined on the basis of an analysis able to consider all the mechanisms affecting heat transfer in the whole CZ furnace, namely a "global analysis of heat transfer", as shown by Derby, Atherton and Gresho (1989); Derby and Xiao (1991); Tsukada, Hozawa and Imaishi (1994). When semitransparent oxide crystals are considered, the influence of the radiative heat transfer in the crystal on the crystal growth behavior must be also modeled within the framework of the global analysis of heat transfer [see Xiao and Derby (1993, 1994); Tsukada, Kakinoki, Hozawa and Imaishi (1995); Kobayashi, Hagino, Tsukada and Hozawa (2002); Yuferev, Budenkova, Vasiliev, Rukolaine, Shlegel, Vasiliev and Zhmakin (2003); Hayashi, Kobayashi, Jing, Tsukada and Hozawa (2004)].

Since the Prandtl number of oxide melts is relatively high, the convection strongly affects the heat transfer in the melt, and consequently, the melt/crystal interface shape.

In the CZ crystal growth of oxides, it is well known that the melt/crystal interface changes abruptly from convex to concave toward the melt as the crystal rotation rate or crystal diameter increases. This abrupt change, called "interface inversion", is attributed to the change of the dominant melt flow near the interface from free convection to forced convection driven by crystal rotation. The cause-effect relationship between melt convection and interface inversion has been investigated numerically in many previous works [Tsukada, Imaishi and Hozawa (1988); Kopetsch (1990); Derby and Xiao (1991); Tsukada, Hozawa and Imaishi (1994)], because the interface shape during the crystal growth is closely related to the crystal quality as mentioned above. The recent global analyses of heat transfer have also demonstrated the effect of the radiative heat transfer in the crystal on the interface inversion [Xiao and Derby (1993, 1994); Kobayashi, Hagino, Tsukada and Hozawa (2002); Hayashi, Kobayashi, Jing, Tsukada and Hozawa (2004)].

The flow mode of the melt is dependent on the temperature profile in the furnace. Often the temperature and velocity fields in the melt become three-dimensional and time dependent, particularly when the size of the crucible is relatively large. The spatial distributions of dopants and defects in the grown crystals, which affect the optical properties and degradation of the oxide crystal, are dependent on the amplitude of temperature and dopant concentration fluctuations at the melt/crystal interface, which is mainly caused by the flow instability. Therefore, the characteristics of the flow instabilities, their origin and critical conditions for their incipience should be well understood so as to fabricate high-quality crystals.

It is relatively easy to observe experimentally the flow patterns on the free surface due to the flow instability. For instance, Takagi, Fukazawa and Ishii (1976), Whiffin, Bruton and Brice (1976), and Brandle (1977) reported that the so-called spoke patterns and wave patterns were seen on the free surface in some oxide melts. Concerning the spoke patterns, many efforts have been made to reveal the mechanism. Miller and Pernell (1981, 1982) performed some experiments using water as a simulated garnet melt and reported that the thermocapillary instability could be an indispensable factor in forming the spoke patterns. This inference was supported by Hurle (1983), Shigematsu, Anzai, Morita, Yamada and Yokoyama (1987), and Morita, Sekiwa, Toshima and Miyazawa (1993). Recently, Jing, Imaishi, Yasuhiro and Miyazawa (1999), Jing, Imaishi, Sato and Miyazawa (2000), Jing, Imaishi, Yasuhiro, Sato and Miyazawa (2000), Jing, Kobayashi, Tsukada, Hozawa, Fukuda, Imaishi, Shimamura, and Ichinose (2003), and Jing, Hayashi, Kobayashi, Tsukada, Hozawa, Imaishi, Shimamura, and Ichinose (2003) demonstrated numerically that the thermocapillary instability could be an indispensable factor in forming the spoke patterns, by carrying out three-dimensional unsteady state analyses of melt convection with the thermocapillary effect on the melt surface. Concerning the wave patterns, Jones (1983, 1984a, 1984b, 1989) took water and a mixture of water and glycerol as working fluids and built many cold model experiments for melt convection in the CZ crucible. He presented some interesting wave patterns seen on the free surface of the cold model fluid and attributed the cause of the wave patterns to the baroclinic instability. Recently, Enger, Basu, Breuer and Durst (2000) first succeeded in numerically reproducing the wave patterns reported by Jones. However, from the viewpoint of the crystal growth, their model corresponding to a cold environment is not sufficient, and thus the radiative heat loss from the free surface should be taken into account. Therefore, in order to understand the oxide melt flows in a realistic CZ crystal growth, Jing, Tsukada, Hozawa, Shimamura, Ichinose and Shishido (2004) simulated numerically the wave pattern on the $LiNbO_3$ melt in a large-scale crucible, and then suggested that the cause of the pattern could be attributed to the baroclinic instability, comparing with the experiments of Lee and Chun (1999).

In the present paper, we survey our recent numerical studies for the CZ crystal growth of oxide. First, we describe the numerical results using the global heat transfer model for an oxide CZ furnace inductively heated by Radio Frequency (RF) ac current, particularly the effect of the internal radiation within the crystal and/or melt on the CZ crystal growth process. Second, the numerical results of unsteady, three-dimensional flows, i.e., the spoke pattern and wave pattern generated on the melt surface, are shown and the origins of their patterns are discussed from view points of buoyancy, thermo-capillary and baroclinic instabilities.

2 Mathematical model

2.1 Global heat transfer analysis

The CZ growth of an oxide crystal by RF induction heating as shown in Fig.1 is considered here. The ac electric current in the coil induces the eddy current in the metal crucible wall, and consequently, the raw material of the crystal inside the crucible is melted by the Joule heating from the eddy current. Therefore, in the global analysis of heat transfer in the inductively heated CZ furnace, first the electromagnetic field in the system should be computed to obtain the distributions of the eddy current, i.e., heat power in the crucible and the after heater; then flow and temperature fields in the furnace as well as the shapes of the melt/crystal and melt/gas interfaces should be calculated. Moreover, if necessary, the thermal stress fields in the crystal which is closely related to the crystal quality, particularly the crack formation in the crystal, can be calculated according to the temperature distributions obtained by the global model. For brevity, mathematical details of calculating the electromagnetic field in the furnace are not included here, but are available in our previous work [Tsukada, Hozawa and Imaishi (1994)]. In calculations, we assume 1) all structures are axisymmetric, 2) temperature and flow fields are in a pseudo-steady state, 3) the melt is Newtonian and the flow is laminar, 4) the Marangoni effect on the melt surface is absent, 5) heat transfer to the surroundings is controlled by radiation alone and the convective heat loss is negligible, and 6) the crystal and/or melt are semitransparent.

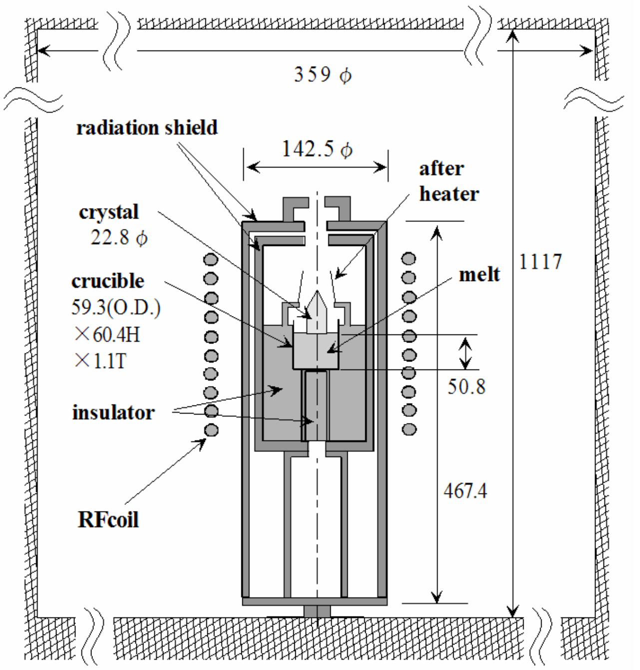

Figure 1 : Schematic diagram of the inductively heated CZ furnace (lengths are in mm)

The dimensionless forms of the governing equations of melt convection, i.e., the continuity equation and the momentum equation based on the Boussinesq approximation, are expressed as follows.

$$\nabla \cdot \boldsymbol{v}_l = 0, \tag{1}$$

$$\boldsymbol{v}_l \cdot \nabla \boldsymbol{v}_l = -\nabla p_l - \nabla \cdot \boldsymbol{\tau}_l + Gr(T_l - 1)\boldsymbol{e}_z. \tag{2}$$

Here, Gr is the Grashof number defined by $\beta' g' T'_m r'^3_c / \nu'^2_l$. The length is scaled with the crucible radius r'_c, velocity with ν'_l / r'_c, the pressure and viscous stress with $\rho'_{0l} \nu'^2_l / r'^2_c$, and the temperature with the melting point temperature T'_m, in which the superscript " $'$" refers to the dimensional value.

The dimensionless energy equations, for instance, for the semitransparent crystal and the opaque melt and other solid structures in the furnace, are given as follows.

Crystal:

$$Pe\,\boldsymbol{e}_z \cdot \nabla T_s = \kappa_s \nabla^2 T_s + a_s N_R \left(J_s - 4n_s^2 T_s^4\right) \tag{3}$$

Melt:

$$Pr\,\boldsymbol{v}_l \cdot \nabla T_l = \nabla^2 T_l \tag{4}$$

Crucible and after heater:

$$\kappa_j \nabla^2 T_j + \alpha Q_0 = 0 \qquad (j = c, h) \tag{5}$$

Elsewhere:

$$\kappa_j \nabla^2 T_j = 0 \tag{6}$$

Pe, Pr and κ_i, are the Peclet number, Prandtl number and thermal conductivity ratios to that of the melt, defined by $\rho'_{0,s}C'_{ps}V'_s r'_c/k'_l$, $\mu'_l C'_{pl}/k'_l$ and k'_j/k'_l, respectively. Q_0 is the dimensionless heat generation rate by the Joule heat in the crucible and after heater for a reference value of the electric current (I'_0) in the RF coil, and is obtained from the analysis of the electromagnetic field in the furnace. In the global analysis, α is determined as a part of the solutions so as to make the temperature at the tri-junction to be at the melting point.

In Eq. (3), the second term on the right-hand side represents the contribution of the internal radiative heat transfer, in which a and N_R are the optical thickness and radiation-conduction interaction parameter defined by $a'r'_c$ and $\sigma' T'^3_m r'_c/k'_l$, respectively. Here, the optical absorption coefficient a' is independent of the wavelength, since we consider the radiative heat transfer in gray absorbing-emitting media. n_s is the refractive index of the crystal. J is the irradiance defined by the zeroth-order moment of radiative intensity I, i.e.,

$$J = \int_{\omega=4\pi} I d\omega. \tag{7}$$

The radiative intensity I is governed by the equation of transfer which represents the radiative heat transfer in an absorbing-emitting, nonscattering medium. Here, to solve the radiative transfer equation, we adopt either the "P_1" approximation [Matsushima and Viskanta (1990); Modest (1993); Tsukada, Kakinoki, Hozawa and Imaishi (1995); Kobayashi, Hagino, Tsukada and Hozawa (2002)] or the finite volume method (FVM) [Liu, Shang and Chen (2000); Hayashi, Kobayashi, Jing, Tsukada and Hozawa (2004)]. The governing equations of P_1 model for the crystal are given as follows,

$$\frac{1}{3a_s}\nabla^2 J_s = a_s \left(J_s - 4n_s^2 T_s^4\right), \tag{8}$$

where J is scaled with $\sigma' T'^4_m$ (note that J was scaled with $4\sigma T'^4_m$ in the previous paper [Kobayashi, Hagino, Tsukada and Hozawa (2002)]. While, if the FVM is used to evaluate the radiative heat transfer, a series of the equations of transfer along discrete directions is solved, where the 4π angular domain at any spatial location is divided into a finite number of discrete, M, nonoverlapping solid angles by the azimuthal discretization strategy. With the discretization of the angular domains, the radiative transfer equation along a specified discrete direction ω^m can be expressed as follows,

$$\frac{\mu^m}{r}\frac{\partial (rI^m)}{\partial r} - \frac{1}{r}\frac{\partial (\eta^m I^m)}{\partial \phi} + \xi^m \frac{\partial I^m}{\partial z} = -a_s I^m + a_s I_b. \tag{9}$$

Here, μ^m, η^m and ξ^m are the direction cosines along the cylindrical coordinates, and ϕ is the azimuthal angle measured from the r-direction. I_b is the blackbody radiant intensity at the temperature of the medium.

The boundary conditions for the system with opaque melt and semitransparent crystal are given by the following equations.

At the melt/crystal interface:

$$\boldsymbol{v}_l \cdot \boldsymbol{n}_{ls} = \boldsymbol{v}_l \cdot \boldsymbol{t} = 0,\ \boldsymbol{v}_l \cdot \boldsymbol{e}_\theta = rRe,\ T_l = T_s = 1 \tag{10a-e}$$

(for P_1 model)

$$-\nabla T_l \cdot \boldsymbol{n}_{ls} + \kappa_s \nabla T_s \cdot \boldsymbol{n}_{ls} = -\frac{\varepsilon_{ls} N_R}{2(2-\varepsilon_{ls})}(J_s - 4n_s^2 T_s^4) - PeSt(\boldsymbol{e}_z \cdot \boldsymbol{n}_{ls}) \tag{10f}$$

$$-\frac{1}{3a_s}\nabla J_s \cdot \boldsymbol{n}_{ls} = -\frac{\varepsilon_{ls}}{2(2-\varepsilon_{ls})}\left(J_s - 4n_s^2 T_s^4\right), \tag{10g}$$

(for FVM)

$$-\nabla T_l \cdot \boldsymbol{n}_{ls} + \kappa_s \nabla T_s \cdot \boldsymbol{n}_{ls} = N_R \sum_{m'}^{M} I^{m'} D^{m'} \omega^{m'} - PeSt(\boldsymbol{e}_z \cdot \boldsymbol{n}_{ls}) \tag{10h}$$

$$I^m = n_s^2 \varepsilon_{ls} T_s^4 + \rho_{ls} \sum_{D^{m'} \rangle 0}^{M} I^{m'} D^{m'} \omega^{m'} (D^m < 0). \tag{10i}$$

At the melt/gas interface:

$$\boldsymbol{v}_l \cdot \boldsymbol{n}_{lg} = 0, \quad \boldsymbol{\tau}_l : \boldsymbol{n}_{lg}\boldsymbol{t} = \boldsymbol{\tau}_l : \boldsymbol{n}_{lg}\boldsymbol{e}_\theta = 0, \tag{11a-c}$$

$$-\nabla T_l \cdot \boldsymbol{n}_{lg} = \varepsilon_{\rm lg}^{out} N_R \left(T_l^4 - q_{i,l}^{out}\right), \tag{11d}$$

At the crucible wall:

$$\boldsymbol{v}_l \cdot \boldsymbol{n}_{lc} = \boldsymbol{v}_l \cdot \boldsymbol{t} = \boldsymbol{v}_l \cdot \boldsymbol{e}_\theta = 0, \tag{12a-c}$$

$$\nabla T_l \cdot \boldsymbol{n}_{lc} = \kappa_c \nabla T_c \cdot \boldsymbol{n}_{lc}, \tag{12d}$$

At the crystal surface:

$$\nabla T_s \cdot \boldsymbol{n}_{sg} = 0, \tag{13a}$$

(for P_1 model)

$$-\frac{1}{3a_s} \nabla J_s \cdot \boldsymbol{n}_{sg} = \frac{1}{2} \left(\frac{1-\rho_{sg}^{in}}{1+\rho_{sg}^{in}} \right) \left(J_s - 4n_s^2 q_{i,s}^{out}\right), \tag{13b}$$

(for FVM)

$$I^m = \tau_{sg}^{out} q_{i,s}^{out} + \rho_{sg}^{in} \sum_{D^{m'} > 0}^{M} I^{m'} D^{m'} \omega^{m'}, \quad (D^m < 0) \tag{13c}$$

Elsewhere:

$$-\kappa_j \nabla T_j \cdot \boldsymbol{n}_{jg} = \varepsilon_{jg}^{out} N_R \left(T_j^4 - q_{i,j}^{out}\right), \tag{14}$$

where $Re = r_c'^2 \omega' / \nu_l'$ and $St = \Delta H_f' / C_{ps}' T_m'$ are the Reynolds number based on the crystal rotation rate and the Stefan number, respectively. In Eq.(11-b), we ignore the thermocapillary (Marangoni) effect on the melt/gas interface. If the effect is considered, however, the tangential force balance on the interface in Eq.(11-b) becomes;

$$\boldsymbol{\tau}_l : \boldsymbol{n}_{lg}\boldsymbol{t} = Ma \nabla T \cdot \boldsymbol{t}, \tag{15}$$

where Ma is the Marangoni number defined by $(-d\gamma'/dT')T_m' r_c' / \rho_{0l}' \nu_l'^2$.

If the melt is semitransparent, the term representing the radiative heat transfer must be added to Eq.(4) as follows,

$$Pr\, \boldsymbol{v}_l \cdot \nabla T_l = \nabla^2 T_l + a_l N_R \left(J_l - 4n_l^2 T_l^4\right), \tag{16}$$

and the boundary conditions at the melt/crystal and melt/gas interfaces and at the crucible wall are also replaced by the appropriate boundary conditions [Kobayashi, Hagino, Tsukada and Hozawa (2002)].

In the CZ crystal growth system, each material constituting the furnace, such as the melt, the crystal and the crucible, is surrounded by a transparent gas, and the incident radiative heat flux to their surfaces through the ambient gas, i.e., irradiation q_i^{out}, is partially absorbed and reflected if the material is opaque. In the case of the semitransparent material, moreover, a part of the irradiation transmits inside the material. Thus, the boundary conditions, Eqs. (11d), (13b,c) and (14), include q_i^{out}. The superscripts "*out*" and "*in*" refer to the outside and inside of the surface adjoining the surrounding gas, respectively, and the subscript "*i*" of q_i^{out} implies the incident flux.

To solve the above governing equations, Eqs.(1)-(6), (8), (9) and (16) with the boundary conditions, Eqs.(10)-(15), q_i^{out} should be given explicitly. Here, we consider that the gas phase in the CZ furnace shown in Fig.1 is the enclosure surrounded by N opaque and semitransparent diffuse-gray surfaces of uniform temperature. The irradiation onto a surface j, $q_{i,j}^{out}$, is given by the following equation, creating an energy balance regarding the surface j in the enclosure:

$$q_{i,j}^{out} = \frac{1}{1-\rho_j^{out}} \left(\varepsilon_j^{out} T_j^4 + \tau_j^{in} q_{i,j}^{in} - q_j\right), \tag{17}$$

where $q_{i,j}^{in}$ is the incident radiative heat flux on the inside of a semitransparent surface j, such as the crystal surface, and is expressed with the irradiance J or radiative intensity I as

(for P_1 model)

$$q_{i,j}^{in} = \frac{J_j}{4} - \frac{1}{6a_j} \nabla J_j \cdot \boldsymbol{n}_{jg} \tag{18a}$$

(for FVM)

$$q_{i,j}^{in} = \sum_{D^{m'} \rangle 0} I^{m'} D^{m'} \omega^{m'} \tag{18b}$$

In addition, the net radiative heat flux at surface j, q_j in Eq.(17), is obtained as a solution of the following matrix equations which describe the balance of radiative heat fluxes in the enclosure:

$$\left(\frac{1}{1-\rho_j^{out}}\right) q_j - \sum_{k=1}^{N} \frac{\rho_k^{out}}{1-\rho_k^{out}} F_{jk} q_k = \frac{1}{1-\rho_j^{out}}(\varepsilon_j^{out} T_j^4 + \tau_j^{in} q_{i,j}^{in}) - \sum_{k=1}^{N} \frac{1}{1-\rho_k^{out}} F_{jk} (\varepsilon_k^{out} T_k^4 + \tau_k^{in} q_{i,k}^{in}) \quad (j=1,2,\ldots,N), \tag{19}$$

where F_{jk} is the view factor. We proposed an efficient method for calculating the view factors in an axisymmetric system by combining the analytical solutions [Tsukada, Hozawa and Imaishi (1994)]. If the material of surface j is opaque, the transmissivity τ_j in Eqs.(17) and (19) is set to be zero, while the emissivity ε_j is neglected in the case of semitransparent materials.

The melt/crystal interface shape is determined so that Eqs.(10d and e) are satisfied, i.e., so that the interface coincides with the melting point isotherm. In addition, the melt/gas interface shape is calculated by solving the non-dimensional Young-Laplace equation.

The finite element method has been used for the calculations of the temperature field in the furnace and velocity field in the melt, as well as for the shapes of the melt/crystal and melt/gas interfaces. The SUPG (streamline upwind Petrov-Galerkin) method [Brooks and Hughes (1982)] can be applied for the treatment of the convective term. The calculation domain is discretized by isoparametric quadrilateral elements, and in each element, velocity vectors, temperature and irradiance are approximated with bilinear polynomials and the pressure is considered to be constant. The details of numerical procedure in the global heat transfer analysis are available in our previous studies [Kobayashi, Hagino, Tsukada and Hozawa (2002); Hayashi, Kobayashi, Jing, Tsukada and Hozawa (2004)]. Only in the numerical simulation of Eq.(9) for the radiative heat transfer, the control volume method was used as numerical procedure.

When the distribution of the thermal stresses in the crystal is needed, a three-dimensional finite element analysis of thermal stress fields can be carried out. Here, the crystal is assumed to be a linear elastic material whose mechanical properties, i.e., elastic constant and thermal expansion coefficient, are anisotropic. The von Mises equivalent stresses in the crystals can be calculated with the temperature distributions obtained by the global heat transfer analysis in the CZ furnace. The mathematical details of calculating the thermal stress fields in the crystal are also available in our previous studies [Miyazaki, Uchida, Tsukada and Fukuda (1996); Kobayashi, Tsukada and Hozawa (2002)].

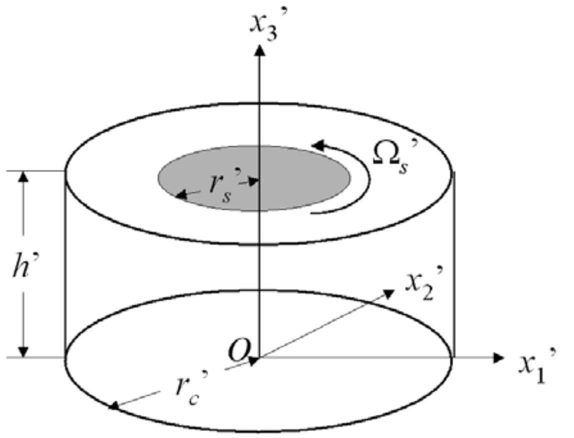

Figure 2 : Coordinate system in three-dimensional unsteady state analysis of melt convection

2.2 *Three-dimensional unsteady state analysis of the oxide melt convection*

To investigate the origins of the spoke pattern and wave pattern generated on the oxide melt surface, a three dimensional unsteady state analysis of melt convection is needed. Since the present status of the “global model” does not permit three-dimensional unsteady global simulation, however, such an investigation has been limited to the crucible with a simple cylindrical geometry depicted in Fig.2. In calculations, the free surface of the melt and the melt/crystal interface are treated as flat, where the temperature of the melt/crystal interface is maintained at the melting point. The heat loss from the free surface of the melt is assumed to be due to radiation alone to an ambient temperature. In most cases, the sidewall of the crucible is heated by a constant and uniform heat flux or is kept at a constant temperature. The bottom of the crucible is adiabatic. The no-slip condition is used for all physical boundaries of the melt except for the free surface. The free surface is considered to be free of stresses or not according to the fact that the Marangoni effect is taken into account in some cases. Under the above assumptions, Eqs.(1), (2), (4) or (16) are solved using the finite difference method.

3 Global simulation of heat transfer in CZ furnace

In this section, the effect of variations in the absorption coefficients, i.e., internal radiation, of the oxide crystal and/or melt, on the interface inversion as well as the thermal stress field in the crystal is discussed on the basis of the global model [Kobayashi, Hagino, Tsukada and Hozawa (2002); Kobayashi, Tsukada and Hozawa (2002)]. We consider the melt flow, heat transfer and melt/crystal interface shape in an inductively heated CZ furnace with 4.6 kHz radio-frequency current, as shown in Fig.1, where a $LiNbO_3$ single crystal (22.8mm diameter) is pulled continuously at the rate of 4 mmh^{-1} from the melt in a Pt crucible (59.3 $mm^{O.D.}\times$60.4 $mm^{H}\times$1.1mm^{T}). Using the thermo physical properties of $LiNbO_3$ melt [Tsukada, Hozawa and Imaishi (1994)], the Prandtl number Pr and the Grashof number Gr in this system are 13.6 and 4.67×10^5, respectively. In addition to the physical properties, the optical properties of the melt and crystal, that are necessary in calculations of internal radiative heat transfer, i.e., the transmissivities on both sides of the semitransparent melt and crystal surfaces, were estimated with the refractive indices ($n_l = n_s$=2.3) [Spuckler and Siegel (1992, 1994)]. On the other hand, when the melt is opaque, the emissivity of the melt into the gas phase was estimated to be 0.80 using the same equation as that for transmissivity, and also the emissivity into the crystal was set to 1.0 because n_l was assumed to be equal to n_s. Since the absorption coefficients of the melt and crystal are not well known, especially at high temperature, we adopted these values as disposable parameters.

Since the following results shown in Figs.3 to 7 were obtained being based on the P_1 approximation for the radiative transfer equation, we must point out that the results should be limited to the case of a medium with a relatively large optical thickness, i.e., a_s or $a_l > 1$.

Fig.3 shows the effect of the crystal rotational Reynolds number Re, the non-dimensional crystal rotation rate, on the temperature distributions in the furnace and the flow pattern in the melt for two values of optical thickness of the crystal a_s, where the melt is opaque, i.e., $a_l = \infty$. The stream functions in the figures are scaled with $r'_c\nu'_l$. When the crystal is not rotated, i.e., Re=0, only the clockwise vortex caused by free convection is present in the melt, and the flow pattern exhibits an undulating structure at the bottom of the crucible due to a retarding force caused by the vertical stratification of the melt. For Re=280, the flow pattern in the melt is almost the same as that for Re=0 in the case of an optically thinner crystal (a_s=1), but a counterclockwise vortex due to crystal rotation exists under the crystal, in addition to free convection, when the optical thickness is large, i.e., a_s=100. Consequently, the interface inversion occurs for optically thicker crystal, but not for optically thinner one at Re=280. The melt convection affects the temperature distributions in the melt and crystal, but the influence of the radiative heat transfer within semitransparent crystals is still more significant. The figures show that the temperature gradients in the crystal decrease when the optical thickness decreases, because the contribution of the radiation to the total heat transfer through the crystal increases and the role of the thermal conduction diminishes. The larger heat flux due to the radiation through the crystal brings about the larger heat flux to the melt/crystal interface from the melt to compensate it. Consequently, the power of the RF coil becomes large, and the melt/crystal interface increases its area and becomes more convex toward the melt.

The effect of the crystal rotational Reynolds number Re on the melt/crystal interface shapes are shown in Figs.4 (a) and (b) for four different values of optical thickness of the crystal, when $a_l = \infty$. In these figures, $\Delta z|_{r=0}$ in (a) represents the axial displacement of the interface at the centerline from the axial position of the melt/crystal/gas tri-junction ($r = r_s$), and $\Delta z|_{r=0.5rs}$ in (b) denotes the axial displacement at the half position of the crystal radius. If both $\Delta z|_{r=0}$ and $\Delta z|_{r=0.5rs}$ are negative, the interface shape is completely convex toward the melt. For all a_s, $\Delta z|_{r=0}$ and $\Delta z|_{r=0.5rs}$ increase with Re, and the melt/crystal interface shape changes from convex to a doubly curved, in other words ‘gull-wing’ or ‘M’ shape, and then becomes completely concave toward the melt, where the doubly curved interface corresponds to the case that satisfies the following relations, $\Delta z|_{r=0} < \Delta z|_{r=0.5rs}$ and $\Delta z|_{r=0.5rs} > 0$. Fig.4 demonstrates numerically that the interface inversion occurs with the increase of Re. When Re is relatively small and the interface is convex toward the melt, the magnitude of the interface deflection $\Delta z|_{r=0}$ becomes larger (more convex toward the melt) as the optical thickness of the crystal a_s decreases, and consequently critical Reynolds number at which the interface inversion occurs, Re_c, shifts to a larger value. In addition, $d\Delta z|_{r=0}/dRe$

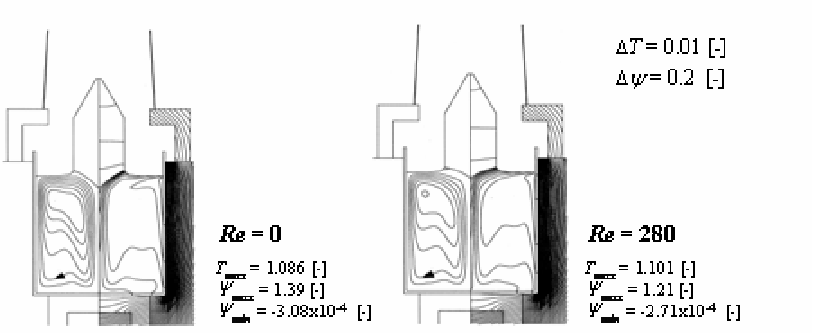

(a) $a_s = 1,\ a_l = \infty$

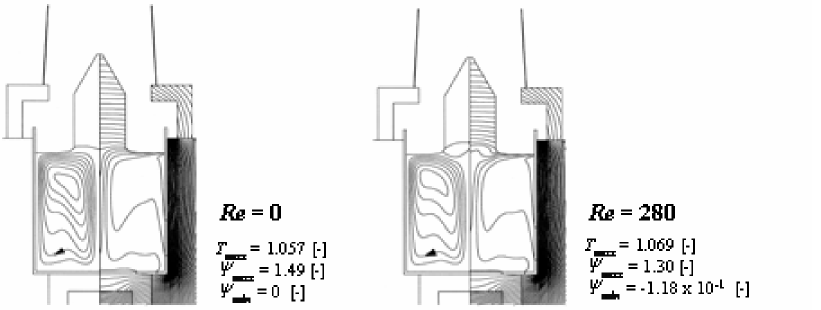

(b) $a_s = 100,\ a_l = \infty$

Figure 3 : Effect of the crystal rotational Reynolds number on the temperature distributions in the furnace and the flow pattern in the melt, when the crystal is semitransparent and the melt is opaque.

and $d\Delta z|_{r=0.5rs}/dRe$ near Re_c increases remarkably as a_s decreases, and thus the interface shape changes more abruptly. These steep increases of $\Delta z|_{r=0}$ and $\Delta z|_{r=0.5rs}$ are due to the melt flow toward the melt/crystal interface caused by the crystal rotation. However, as Re increases further beyond Re_c, the difference between $\Delta z|_{r=0}$ and $\Delta z|_{r=0.5rs}$ for the same Re and their dependence of Re become smaller. Also, the differences of $\Delta z|_{r=0}$ and $\Delta z|_{r=0.5rs}$ between the each case of a_s becomes smaller.

Here, the thermocapillary (Marangoni) convection is not taken into account. However, it is expected that the critical Reynolds number for the interface inversion should become larger in the presence of the thermocapillary force because it tends to strengthen the buoyancy driven flow and to suppress the appearance of the centrifugal-force-driven flow related to the crystal rotation [Tsukada, Hozawa and Imaishi (1994)].

Since some experimental studies [Okano, Tsuji, Yoon, Hoshikawa and Fukuda (1994)] revealed the possibility of the influence of the radiative heat transfer in the melt on the crystal growth processes, particularly on the melt convection, the effect of the crystal rotation on the CZ crystal growth process should be investigated when both melt and crystal are semitransparent. Along these lines, Fig.5 shows the effect of the crystal rotational Reynolds number Re on the temperature distributions in the furnace and the flow pattern in the melt for two values of optical thickness, where $a_l = a_s$. In the case of optically thicker melt and crystal, i.e., $a_l = a_s$=100, the shapes of the temperature distributions and flow patterns are almost the same as those in Fig.3, and the interface inversion occurs as Re increases. However, for $a_l = a_s$=1 and Re=0, compared with the results for $a_l = a_s$=100, the undulating flow structure near the crucible bottom disappears, and a relatively simple convection with the vortex center at the middle part of the melt occurs. In addition, the intensity of the convection in the melt is larger despite the decrease of the maximum temperature in the melt. The radiative energy emitted at the crucible wall is absorbed inside the melt and heats it. Also, the contribution of radiation to the total heat loss through the melt becomes larger, and the conduction becomes less significant. Consequently, vertical density stratification of the melt disappears, but the horizontal temperature gradient in the melt drives the

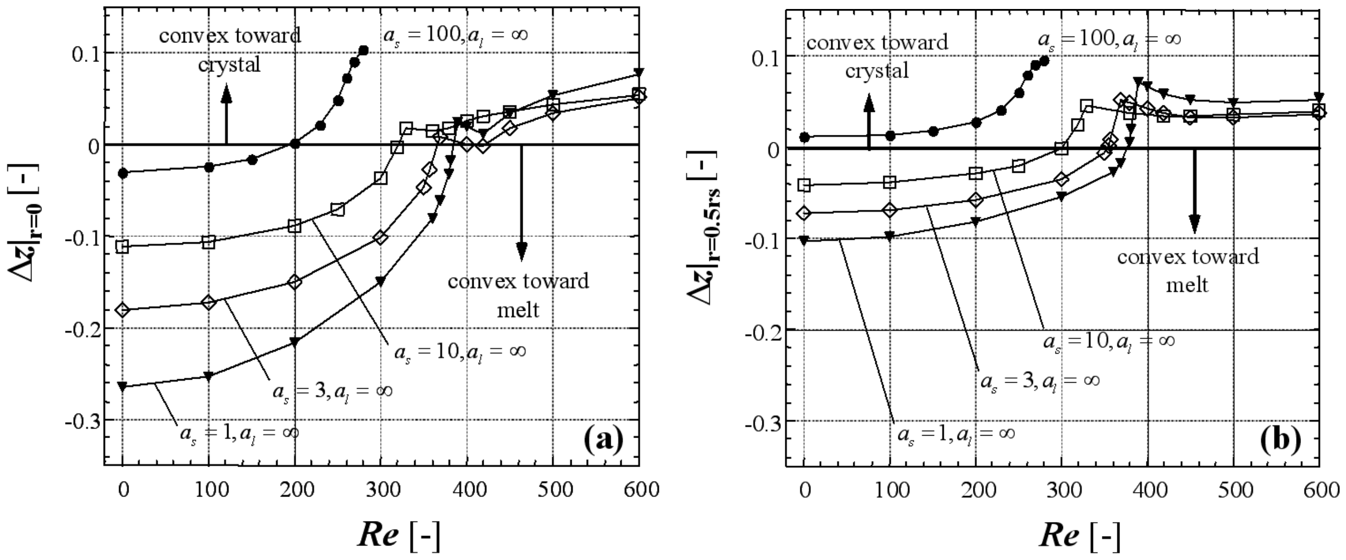

Figure 4 : Effect of the crystal rotational Reynolds number on the melt/crystal interface shape when the crystal is semitransparent and the melt is opaque.

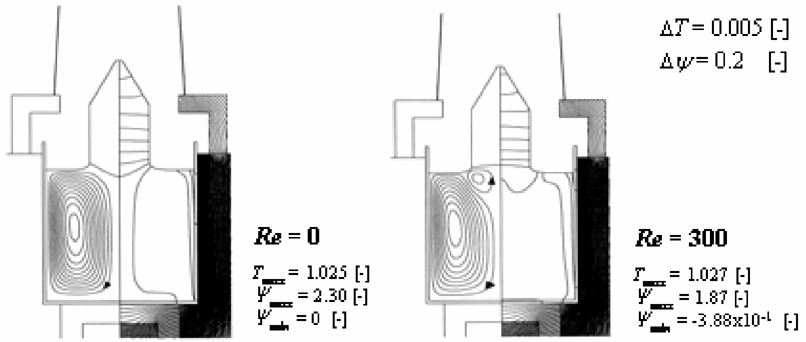

(a) $a_s = a_l = 1$

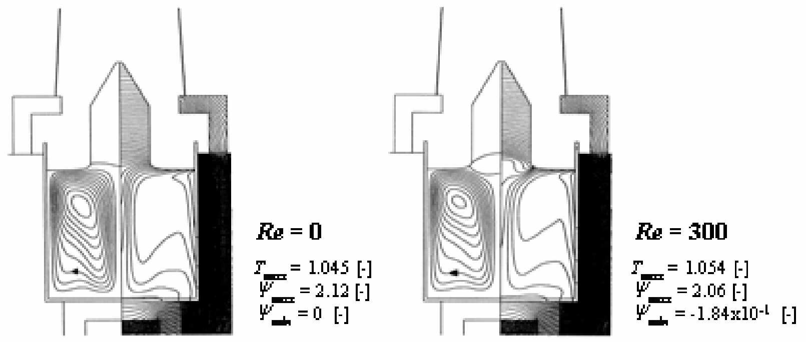

(b) $a_s = a_l = 100$

Figure 5 : Effect of the crystal rotational Reynolds number on the temperature distributions in the furnace and the flow pattern in the melt, when both the crystal and melt are semitransparent.

buoyant flow which is stronger than that in the optically thicker melt. In this case, also, the melt/crystal interface shape becomes more convex toward the melt as the optical thickness of both melt and crystal decreases.

Fig.6 shows the effect of the crystal rotational Reynolds number *Re* on the melt/crystal interface shapes for five different values of optical thickness, when both melt and crystal are semitransparent and $a_l = a_s$. For all a_s, $\Delta z|_{r=0}$ increases in the range of relatively small *Re* and the melt/crystal interface changes from convex to concave toward the melt at Re_c. This trend is similar to that reported in the case of the opaque melt shown in Fig.4 although the gull-wing geometry of the interface has not been clearly observed. However, Re_c for a_s=1 is much smaller than those for a_s=10. With regard to this aspect, comparing the flow patterns in the melt between a_s=1 and 10, it is clear that the intensity of clockwise buoyant flow for a_s=1 is weaker than that for a_s=10. This leads to the decrease of the Re_c at which the dominant melt flow near the interface changes from free convection to forced convection driven by crystal rotation. To sum up the behavior on the shape of the melt/crystal interface, it is clearly found that the Re_c, when the melt is opaque, decreases monotonously with the optical thickness of the crystal, whereas the Re_c shows a maximum value at a certain optical thickness of the crystal and melt when the melt is semitransparent and $a_l = a_s$.

Since the thermal field in the crystal and the melt/crystal interface shape are strongly affected by both the radiative heat transfer in the crystal and the melt convection as mentioned above, it can be inferred that the thermal stresses in the crystal also vary depending on the absorption coefficient of the crystal or the crystal rotation rate. Fig.7 shows the effect of *Re* on the maximum values of the thermal stresses in the crystal for four different values of optical thickness of the crystal when the melt is opaque [Kobayashi, Tsukada and Hozawa (2002)]. In the figure, the dotted lines are the maximum values of the von Mises stresses in the whole crystal and the solid lines are the maxima at the melt/crystal interface. For $a_s = 0.1$ and 1, the maxima always appear at the melt/crystal interface for all *Re*. The results for $a_s = 0.1$ are represented to investigate extensively the effect of optical thickness, although the P_1 approximation to calculate the radiative heat transfer in the crystal is not very suitable for such optically thin crystals. For all a_s, the maximum value of the stresses at the melt/crystal interface decreases with *Re*, and becomes minimum near the critical Reynolds number Re_c, at which the interface is almost flat, i.e., the interface inversion occurs. Beyond Re_c, the thermal stresses increase abruptly with *Re*. When *Re* is relatively small and the interface is convex toward the melt, the magnitude of the thermal stresses at the interface is the largest for $a_s = 1$. This is explained by the competition between the interface deflection $\Delta z|_{r=0}$ and the temperature gradients in the crystal. As the optical thickness decreases, the magnitude of the interface deflection becomes larger and consequently, the radial temperature gradient near the melt/crystal interface becomes larger, but simultaneously, the axial temperature gradient through the crystal becomes smaller because the radiative heat transfer becomes more dominant. In addition, it was found that the dependence of the stresses on the optical thickness for the opaque melt is larger than that for the semitransparent melt [Kobayashi, Tsukada and Hozawa (2002)].

Since the P_1 approximation is not very reliable for optically thin materials to solve the radiative transfer equation, the melt and/or crystal with a relatively thick optical thickness have been considered above. However, it should be emphasized that oxide crystals have a wide range of absorption coefficient values, and depending on their values the contributions of radiation to heat transfer and consequently the melt/crystal interface shape vary, as shown in the previous experimental work [Cockayne, Chesswas and Gasson (1969)]. Therefore, to remove the aforementioned limitation related to the P_1 approximation, the P_1 model has been replaced by the finite volume method (FVM) [Liu, Shang and Chen (2000)] in order to correctly take into account the radiative heat transfer in crystals with a wide range of optical thickness values. Fig.8 shows the effect of the crystal rotational Reynolds number *Re* on the melt/crystal interface shapes for the different values of optical thickness of the crystal [Hayashi, Kobayashi, Jing, Tsukada and Hozawa (2004)]. When $a_s = 10$ and 0.1, $\Delta z|_{r=0}$ increases with *Re*, and the melt/crystal interface shape changes from convex to concave toward the melt. These trends are almost the same as those in Fig.4. In addition, when the optical thickness becomes less than 0.1, it is found that the dependency of the optical thickness on the melt/crystal interface becomes slight.

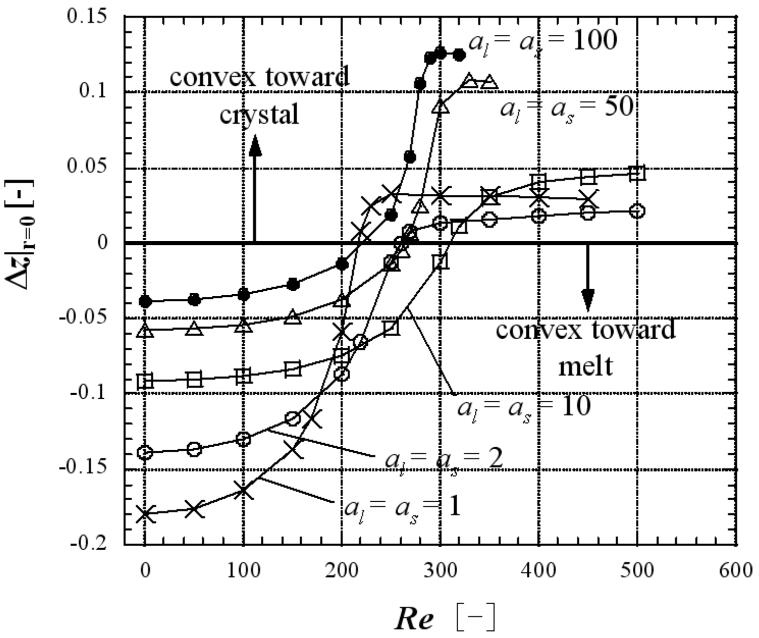

Figure 6 : Effect of the crystal rotational Reynolds number on the melt/crystal interface shape when both the crystal and melt are semitransparent.

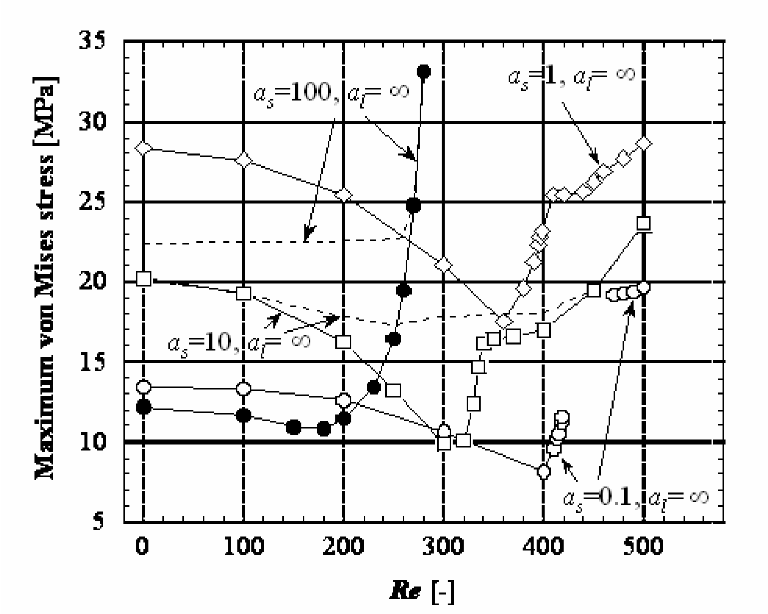

Figure 7 : Effect of the crystal rotational Reynolds number on the maximum von Mises stresses in the crystal (Solid line: at melt/crystal interface, dotted line: in whole crystal).

4 Flow instability in oxide melt

4.1 Marangoni instability

It is well known that asymmetric surface patterns, namely spoke patterns or wave patterns, appear on the surface of oxide melt in the CZ crystal growth configuration. As mentioned in the introduction, it has been disclosed experimentally that the spoke pattern is generated due to the Marangoni instability. Recently, we reproduced the spoke patterns on $LiNbO_3$ melt surface in the CZ system by unsteady three-dimensional numerical simulations of melt convection. The origin of the spoke patters was examined by a set of simulations for open melt, i.e., without crystal, assuming the temperature coefficient of sur-

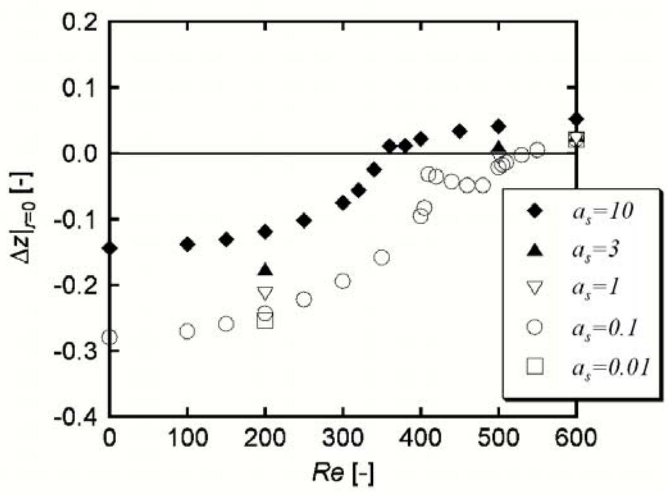

Figure 8 : Effect of the crystal rotational Reynolds number on the melt/crystal interface shape when the crystal is semitransparent and the melt is opaque.

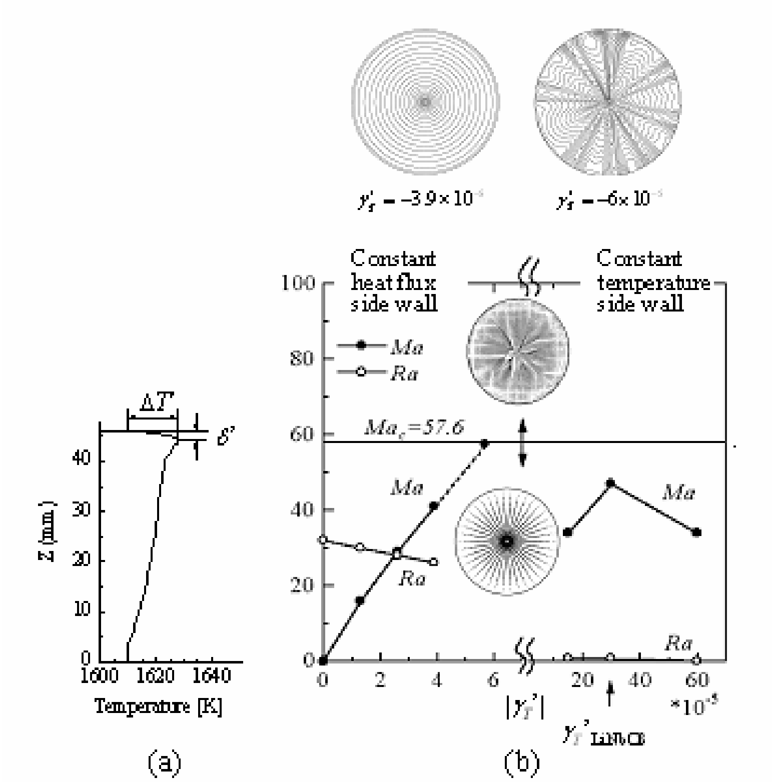

Figure 9 : Criteria of the spoke patterns on open melt surface; (a) axial temperature distribution in the melt, (b) flow diagram in Marangoni instability.

face tension as a disposable parameter [Jing, Imaishi, Yasuhiro and Miyazawa (1999)]. Local values of the Marangoni and the Rayleigh numbers were calculated based on the thickness of the thermal boundary layer, δ', and the temperature drop in the boundary layer, $\Delta T'$, evaluated at $r' = 0.75r_c'$, as shown in Fig. 9(a). In oxide melts, Pr is large and δ' is much thinner than that of semiconductor melts. According to the above mentioned analysis, in the condition of crucible side wall heated with a constant heat flux (Left in Fig.9(b)), the Rayleigh number ranges between 40 and 20, and is too small to initiate the Rayleigh instability in the thermal boundary layer. However, spoke patterns appear when *Ma* exceeds a certain threshold value, suggesting the Marangoni instability in the thermal boundary layer is responsible for the spoke patterns. The threshold value, the critical Marangoni number for the incipience of the instability, is about 60. No linear stability analysis has been conducted for such a flow system. But $Ma_c = 60$ is very close to the critical Marangoni number ($Ma_c = 56.7$) [Higano(1981); Boeck and Thess (1997)] for the incipience of the Marangoni-Bènard convection in an infinitely extended fluid layer bounded by an adiabatic top surface and a bottom wall of free slip and constant temperature. In a super critical condition, Marangoni instability triggers roll cells in the boundary layer. Because of the dominant basic flow in radial direction, the roll-axes are extended in radial direction and aligned as spoke pattern. We believe that the Marangoni instability is indispensable to initiate the spoke patterns. However, for the sake of the completeness, it should be pointed out that Szmyd, Jaszczur, Ozoe and Kakimoto (2000) reported simulation of spoke patterns on a high temperature melt surface where thermocapillary effect was absent. In practice, their patterns are initiated by the Rayleigh instability in a much thicker thermal boundary layer. Generally, thermal boundary layer thickness and temperature drop in it are strongly dependent on the radiative heat loss from the melt surface, on the boundary condition at the side-wall and also on the surface velocity. In some case, spoke pattern can not occur in a crucible with a constant-temperature side-wall which significantly reduces the thermal boundary layer thickness [Jing, Yasuhiro, Suenaga, Sato and Imaishi (2000)].

The effect of the RF coil position on the spoke pattern was investigated numerically by Jing, Kobayashi, Tsukada, Hozawa, Fukuda, Imaishi, Shimamura and Ichinose (2003). The conductive heat transfer in the crucible was taken into account as well as the flow and thermal fields in the melt, according to the distributions of the heat generation rate in the crucible obtained by the analysis of electromagnetic field in the furnace (similar to the global heat transfer analysis). It was revealed that the appearance of spoke pattern is dependent on the RF coil position reflecting the distributions of the heat generation rate in the crucible. When the RF coil was set low with respect to the crucible, the spoke pattern appeared easily, otherwise, the spoke pattern was hard to be obtained, as shown in Fig.10(a) and (b). These results demonstrate that the thermal boundary layer thickness, in other word, the Marangoni number, varies with the distributions of the heat generation rate in the crucible, and support the theory related to the formation mechanism of spoke patterns based on the Marangoni instability.

In addition, we revealed that the optical properties of the melt are also important for the appearance of the spoke patterns [Jing, Hayashi, Kobayashi, Tsukada, Hozawa, Imaishi, Shimamura and Ichinose (2003)]. If the melt is highly transparent, temperature gradient becomes very small throughout the oxide medium because the contribution of internal radiation to heat transfer becomes larger in comparison with conduction. In such a case, secondary flows caused by the Marangoni instabilities in the thermal boundary layer may not occur, thus the spoke pattern can not be observed on the melt surface.

4.2 Baroclinic instabilities in oxide melt

It is well known that asymmetric wavy and unsteady pattern appear on the oxide melt surfaces at medium range of crystal rotation rate. The surface patterns are dependent on the nature of the bulk flow field, where the melt flow is driven by the rotating crystal and the buoyancy. In the absence of Marangoni forces (surface tension effects neglected) the melt below the crystal tends to be sucked upward and expelled out toward the crucible by the centrifugal force induced by the rotating crystal. On the other hand, the melt near the crucible tends to rise along the crucible sidewall and flow towards the crystal along the free surface owing to the buoyancy effect. When the buoyancy-driven flow and crystal rotation-driven flow are of a comparable magnitude, a wave pattern appears on the melt surface. The unsteady three-dimensional numerical simulations for the $LiNbO_3$ melt convection in a large-size cylindrical crucible with radius $r'_c = 100$ mm are discussed below [Jing, Tsukada, Hozawa, Shimamura, Ichinose and Shishido (2004)]. The Grashof number is 2.02×10^7.

Fig. 11(a) shows the grayscale expression of the temperature on the free surface, and (b) and (c) show the meridian view of the isotherms and velocity vectors for the crystal rotation rate $\Omega'_s = 15$ rpm, where a simplified constant heat flux is given at the crucible sidewall

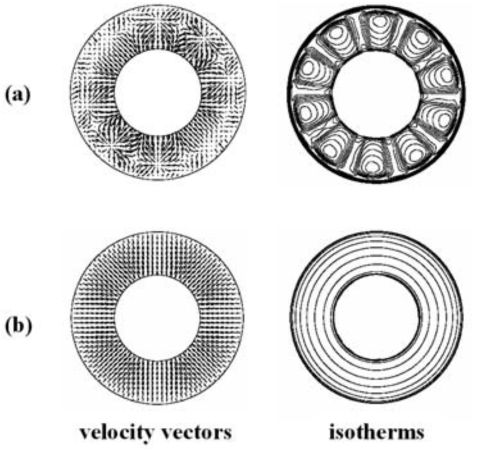

Figure 10 : Effect of RF coil position on the velocity vectors and isotherms on the melt surface, where a RF coil was set (a) low and (b) high with respect to the crucible, respectively.

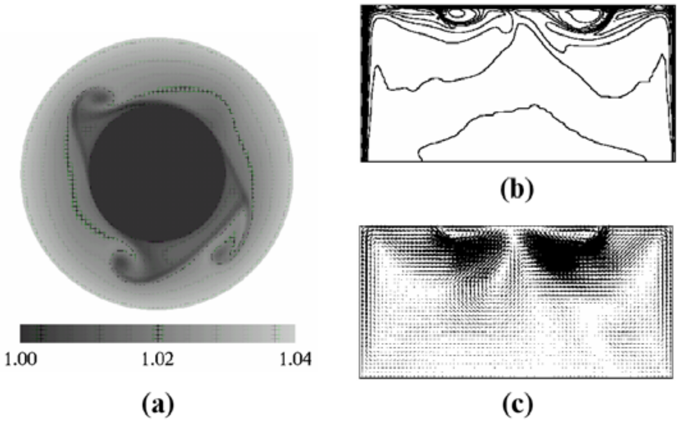

Figure 11 : The grayscale surface wave pattern (a) and the side view of the temperature distribution (b) and the velocity vectors (c) in the crucible.

and the bottom of the crucible is adiabatic. According to the numerical results, a 3-folded wave pattern appears on the melt surface and rotates at the rate of approximately 1 rpm which is completely different from that of crystal rotation. A series of the numerical simulations indicates that no surface pattern can be found when the rotation rate of the crystal is $\Omega'_s < 10$ rpm; whereas, the wave patterns tends to move toward the crucible on the free surface with the increase in the crystal rotation rate and a 4-folded quadrilateral wave patterns occurs for $\Omega'_s = 20$ rpm. Then, when the crystal rotation-driven flow becomes dominant and pushes the buoyancy-driven flow toward the crucible wall, the wave pattern disappears.

One of the causes of the generation of the surface wave patterns is the baroclinic instability, which arises from the interaction between Coriolis and buoyancy forces. This might be supported by comparing the present numerical results with the experimental ones by Lee and Chun (1999), who experimentally determined conditions for the baroclinic instability in the liquid of oxide CZ configuration using the aforementioned cold model fluids. Fig.12 shows the flow regime diagram representing the region of baroclinic wave flows, where Ro_t is the Rossby number, $Ro_t = g'\beta'\Delta T'h'/4\omega_s'^2(r'_c - r'_s)^2$ and Ta the Taylor number, $Ta = 4\omega_s'^2(r'_c - r'_s)^5/\nu'^2h'$. The range of the rotation rates at which the wave patterns were observed in the present simulations when the Marangoni effect was ignored, i.e., the region depicted by the solid squares, falls on the baroclinic wave flow region of Lee and Chun (1999), despite the large difference between the actual oxide melt and the cold model fluid, particularly for the heat loss from the melt surface.

Comparing the temperature distributions for $\Omega'_s = 15$ rpm and $\Omega'_s = 20$ rpm, it can be found that in the former case, the isotherms of relatively low temperatures characterizing the surface wave patterns are scraping the crystal edge and rotating as shown in Fig.11, whereas in the latter case, they are rotating away from the crystal edge. According to the fact that the isotherms in the former case are much close to the melting point T'_m and temperature fluctuations occur in the growth system, the shape of the grown crystal might not be ensured to be cylindrical. Along these lines, it was occasionally reported during growth experiments that a spiral growth can occur for some crystals, where the crystal grows in a spiral or helix shape instead of the correct cylindrical shape. The occurrence of the wave patterns in the former case might be one of the causes of the spiral growth. Consequently, the flow regime diagram in Fig.12 might suggest the appropriate crystal rotation rate at which the spiral growth is suppressed.

In addition, what kind of flow and surface pattern will appear if the Marangoni effect which is the primary cause of spoke patterns is taken into account is even very interesting. Adding the Marangoni effect to the numerical simulation in Fig.11, the wave pattern disappears and no pattern can be generated because the Marangoni effect accelerates the inward flow along the free surface and,

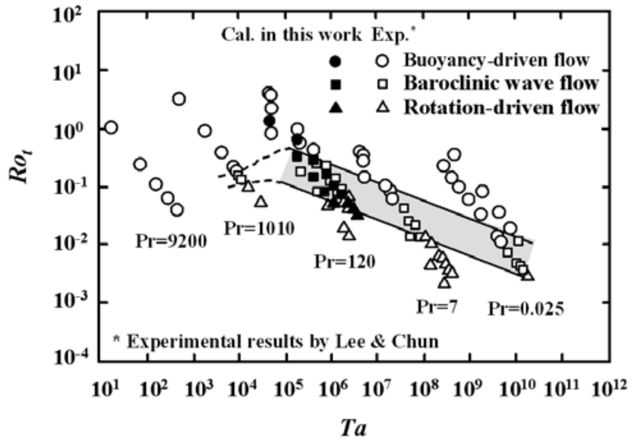

Figure 12 : Flow regime diagram. Baroclinic wave flow regime exists between the buoyancy-driven and the rotation-driven flow regimes.

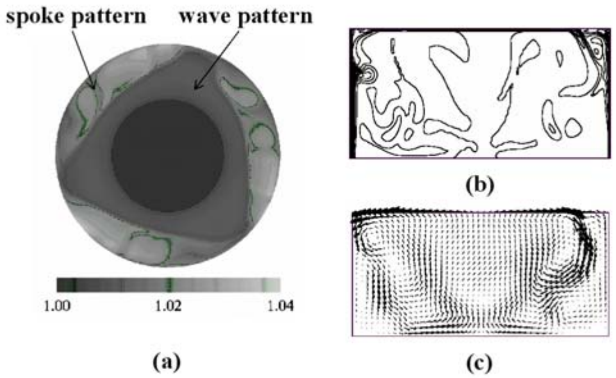

Figure 13 : The grayscale surface wave-spoke pattern (a) and the side view of the temperature distribution (b) and the velocity vectors (c) in the meridian plane.

therefore, suppresses the outward flow driven by the rotating crystal. When the rotation rate of the crystal is increased to $\Omega_s' > 40$ rpm, the outward flow driven by the rotating crystal can overcome the inward flow driven by both buoyancy and the Marangoni effects and push the meeting front onto the free surface again. Fig.13(a) shows the grayscale surface pattern, and Figs. 13(b) and (c) show the bulk temperature distribution and flow in the meridian plane, respectively, for the $\Omega_s' = 41$ rpm. In this case, the spoke pattern induced by the Marangoni instability is also generated between the triangular-shaped wave pattern and the crucible wall. This is the reason why such a surface pattern was named as wave-spoke pattern. The numerical simulations prove that when $\Omega_s' > 45$ rpm, the wave-spoke pattern disappears and the rotation-driven flow becomes dominant. The mechanism for the spoke pattern here is identical to that mentioned in the previous section.

5 Conclusions

In the first part of the present paper we described the latest in the "global" modeling of heat transfer in inductively heated CZ furnaces used to grow oxide single crystals. Particularly, it was emphasized that accounting for the internal radiation within the crystal and/or melt in the model is important because they are often semitransparent to infrared radiation. Some results of the global analyses suggest that the melt/crystal interface shape is strongly affected by the optical properties as well as by the melt convection. Next, convective instability generated in the oxide melt, i.e., spoke pattern and wave pattern, have been discussed within the framework of an unsteady three-dimensional analysis. It has been demonstrated numerically that the spoke pattern is due to a Marangoni instability, while the wave pattern is cased by a baroclinic instability.

Nomenclatures

a = optical thickness	[-]
a' = absorption coefficient	[m^{-1}]
C_p' = heat capacity	[J.kg^{-1}.K^{-1}]
D = product of the unit normal vector at the surface and intensity direction	[-]
$\boldsymbol{e}$ = unit vector	[-]
F_{jk} = view factor	[-]
g' = gravitational acceleration	[m.s^{-2}]
Gr = Grashof number	[-]
$\Delta H_f'$ = latent heat of solidification	[J.kg^{-1}]
h' = melt depth	[m]
I= radiative intensity	[-]
I_0' = electric current	[A]
J = irradiance	[-]
k' = thermal conductivity	[W.m^{-1}.K^{-1}]
Ma = Marangoni number	[-]

Ma_c = critical Marangoni number	[-]
N_R = radiation–conduction interaction parameter	[-]
n = refractive index	[-]
$\boldsymbol{n}$ = normal unit vector	[-]
Pe = Peclet number	[-]
Pr = Prandtl number	[-]
p = pressure	[-]
Q_0= standard volumetric heat generation rate	[-]
q_j = net heat flux due to the incident radiation on jth boundary surface	[-]
$q_{i,j}$ =incident radiative flux on jth boundary surface	[-]
Ro_t = Rossby number	[-]
r = radial position in cylindrical coordinates	[-]
r'_c = crucible radius	[m]
r'_s = crystal radius	[m]
Re = Reynolds number	[-]
Re_c = critical Reynolds number	[-]
St = Stefan number	[-]
T = temperature	[-]
Ta = Taylor number	[-]
T'_m = melting temperature	[K]
$\boldsymbol{t}$ =tangential unit vector	[-]
V'_s = crystal pulling rate	[m.s^{-1}]
$\boldsymbol{v}$ = velocity vector	[-]
x'_1, x'_2, x'_3 = Cartesian coordinates	[m]
z = axial position in cylindrical coordinates	[-]
Δz = axial displacement of the interface	[-]
Greek symbols	
α = heat generation coefficient	[-]
β' = thermal expansion coefficient	[K^{-1}]
δ' = thermal boundary layer thickness	[m]
ε = emissivity	[-]
ϕ = azimuthal angle	[rad]
γ'= surface tension	[N.m^{-1}]
$\gamma_T{}'$= temperature coefficient of surface tension	[N.m^{-1}.K^{-1}]
η = direction cosine along the ϕ-axis.	[-]
κ = ratio of thermal conductivity	[-]
μ = direction cosine along the r-axis	[-]
μ' = viscosity	[Pa.s]
ν' = kinematic viscosity	[m^2.s^{-1}]
ρ'_0 = density	[kg.m^{-3}]
ρ = reflectivity	[-]
σ' = Stefan-Boltzman constant	[W.m^{-2}.K^4]
$\boldsymbol{\tau}$ = stress tensor	[-]
τ = transmissivity	[-]
ψ = stream function	[-]
ξ=direction cosine along the z-axis	[-]
Ω' = crystal rotation rate	[rpm]
ω = solid angle	[sr]
ω' = crystal rotation rate	[s^{-1}]

Superscripts

in= inside of boundary surface

m= discrete direction of solid angle

out = outside of boundary surface

$'$ = dimensional value

Subscripts

b = black body

c = crucible

h = after heater

j = material j

jg = pointing from material j to gas phase

l = melt

lc = pointing from melt to crucible

lg = pointing from melt to gas phase

ls = pointing from melt to crystal

max = maximum value

min = minimum value

s = crystal

sg = pointing from crystal to gas phase

z = z-direction

θ = θ-direction

References

Boeck, T.; Thess, A. (1997): Inertial Benard-Marangoni convection. *J. Fluid Mech.*, vol. 350, pp. 149-175.

Brandle, C. D. (1977): Simulation of fluid flow in $Gd_3Ga_5O_{12}$ melts. *J. Crystal Growth*, vol. 42, pp. 400-404.

Brandle, C. D.; Fratello, V. J.; Valentine, A. J.;

Stokowski, S. E. (1987): Effects of impurities and atmosphere on the growth of Cr-doped gadolinium scandium gallium garnet. I. *J. Crystal Growth*, vol. 85, pp. 223-228.

Brooks, A. N.; Hughes, T. J. R. (1982): Streamline upwind/ Petrov-Galerkin formulations for convection dominated flows with particular emphasis on the incompressible Navier-Stokes equations. *Comp. Meth. Appl. Mech. Engrg.*, vol. 32, pp. 199-259.

Cockayne, B.; Chesswas, M.; Gasson, D. B. (1969): Facetting and optical perfection in Czochralski grown garnets and ruby. *J. Mater. Sci.*, vol. 4, pp. 450-456.

Derby, J. J.; Atherton, L. J.; Gresho, P. M. (1989): An integrated process model for the growth of oxide crystals by the Czochralski method. *J. Crystal Growth*, vol. 97, pp. 792-826.

Derby, J. J.; Xiao, Q. (1991): Some effects of crystal rotation on large-scale Czochralski oxide growth: analysis via a hydrodynamic thermal-capillary model. *J. Crystal Growth*, vol. 113, pp. 575-586.

Enger, S.; Basu, B.; Breuer, M.; Durst, F. (2000): Numerical study of three-dimensional mixed convection due to buoyancy and centrifugal force in an oxide melt for Czochralski growth. *J. Crystal Growth*, vol. 219, pp .144-164.

Hayashi, A.: Kobayashi, M.; Jing, C. J.; Tsukada, T.; Hozawa, M. (2004): Numerical simulation of the Czochralski growth process of oxide crystals with a relatively thin optical thickness. *Int. J. Heat Mass Transfer*, vol. 47, pp. 5501-5509.

Higano, M. (1981): Thermal instability of liquid layer, Part 1, Marangoni instability. *Trans. JSME*, vol. 47, pp. 105-110.

Hurle, D. T. J. (1983): Convective transport in melt growth systems. *J. Crystal Growth*, vol. 65, pp. 124-132.

Jing, C. J.; Imaishi, N.; Yasuhiro, S.; Miyazawa, Y. (1999): Three-dimensional numerical simulation of spoke pattern in oxide melt. *J. Crystal Growth*, vol. 200, pp. 204-212.

Jing, C. J.; Imaishi, N.; Sato, T.; Miyazawa, Y. (2000): Three-dimensional numerical simulation of oxide melt flow in Czochralski configuration. *J. Crystal Growth*, vol. 216, pp. 372-388.

Jing, C. J.; Imaishi, N.; Yasuhiro, S.; Sato, T.; Miyazawa, Y. (2000): Three-dimensional numerical simulation of rotating spoke pattern in an oxide melt under a magnetic field. *Int. J. Heat and Mass Transfer*, vol. 43, pp. 4347-4359.

Jing, C. J.; Yasuhiro, S.; Suenaga, H.; Sato, T.; Imaishi, N. (2000): Numerical simulation of oxide melt flow in a crucible with a constant temperature side wall. *Thermal Science and Engineering*, vol. 8, pp. 1-8.

Jing, C. J.; Kobayashi, M.; Tsukada, T.; Hozawa, M.; Fukuda, T.; Imaishi, N.; Shimamura, K.; Ichinose N. (2003): Effect of RF coil position on spoke pattern on oxide melt surface in Czochralski crystal growth. *J. Crystal Growth*, vol. 252, pp. 550-559.

Jing, C. J.; Hayashi, A.; Kobayashi, M.; Tsukada, T.; Hozawa, M.; Imaishi, N.; Shimamura, K.; Ichinose N. (2003): Effect of internal radiative heat transfer on spoke pattern on oxide melt surface in Czochralski crystal growth. *J. Crystal Growth*, vol. 259, pp. 367-373.

Jing, C. J.; Tsukada, T.; Hozawa, M.; Shimamura, K.; Ichinose, N.; Shishido T. (2004): Numerical studies of wave pattern in an oxide melt in the Czochralski crystal growth. *J. Crystal Growth*, vol. 265, pp. 505-517.

Jones, A. D. W. (1983): An experimental model of the flow in Czochralski growth. *J. Crystal Growth*, vol. 61, pp. 235-244.

Jones, A. D. W. (1984a): Hydrodynamics of Czochralski growth - A review of the effects of rotation and buoyancy. *Progr. Crystal Growth Characterization*, vol. 9, pp. 139-168.

Jones, A.D.W. (1984b): The temperature field of a model Czochralski melt. *J. Crystal Growth*, vol. 69, pp. 165-172.

Jones, A.D.W. (1989): Flow in a model Czochralski oxide melt. *J. Crystal Growth*, vol. 94, pp. 421-432.

Kobayashi, M.; Hagino, T; Tsukada, T.; Hozawa, M. (2002): Effect of internal radiative heat transfer on interface inversion in Czochralski crystal growth of oxides. *J. Crystal Growth*, vol. 235, pp. 258-270.

Kobayashi, M.; Tsukada, T.; Hozawa, M. (2002), Effect of internal radiation on thermal stress fields in CZ oxide crystals. *J. Crystal Growth*, vol. 241, pp. 241-248.

Kopetsch, H. (1990): Numerical simulation of the interface inversion in Czochralski growth of oxide crystals. *J. Crystal Growth*, vol. 102, pp. 505-528.

Kvapil, Ji.; Kvapil, Jo.; Manek, B.; Perner, B.; Au-

trata, R.; Scuer, P. (1981): Czochralski growth of YAG:Ce in a reducing protective atmosphere. *J. Crystal Growth*, vol. 52, pp. 542-545.

Lee, Y. S.; Chun, Ch. H. (1999): Prandtl number effect on traveling thermal waves occurring in Czochralski crystal growth. *Adv. in Space Res.* Vol. 24, pp. 1403-1407.

Liu, J.; Shang, H. M.; Chen, Y. S. (2000): Development of an unstructured radiation model applicable for two-dimensional planar, axisymmetric, and three-dimensional geometries. *J. Quantitative Spectrosc. Radiat. Transfer*, vol. 66, pp. 17-33.

Matsushima, H.; Viskanta, R. (1990): Effect of internal radiation transfer on natural convection and heat transfer in a vertical crystal growth configuration. *Int. J. Heat Mass Transfer*, vol. 33, pp. 1957-1968.

Miller, D. C.; Pernell, T. L. (1981): The temperature distribution in a simulated garnet Czochralski melt. *J. Crystal Growth*, vol. 53, pp. 523-529.

Miller, D. C.; Pernell, T. L. (1982): Fluid flow patterns in a simulated garnet melt. *J. Crystal Growth*, vol. 57, pp. 253-260.

Miyazaki, N.; Uchida, H.; Tsukada, T.; Fukuda, T. (1996): Quantitative assessment for cracking in oxide bulk single crystals during Czochralski growth: development of a computer program for thermal stress analysis. *J. Crystal Growth*, vol. 162, pp. 83-88.

Modest, M. F. (1993): *Radiative Heat Transfer*, McGraw-Hill, New York, pp. 713-724.

Morita, S.; Sekiwa, H.; Toshima, H.; Miyazawa, Y. (1993): The growth of Al_2O_3 single crystals by the Czochralski method. *J. Ceramic Soc. Japan*, vol. 101, pp. 108-112.

Okano, Y.; Tsuji, Y., Yoon, D. H., Hoshikawa, K., Fukuda, T. (1994): Internal radiative heat transfer in Czochralski growth of $LiTaO_3$ single crystal. *J. Crystal Growth*, vol. 141, pp. 383-388.

Shigematsu, K.; Anzai, Y.; Morita, S.; Yamada, M.; Yokoyama, H. (1987): Growth Conditions of Subgrain-Free $LiNbO_3$ Single Crystals by the Czochralski Method. *Jpn. J. Appl. Phys.*, vol. 26, p. 1988-1996.

Spuckler, C. M.; Siegel, R. (1992): Refractive index effects on radiative behavior of a heated absorbing-emitting layer. *J. Thermopysics Heat Transfer*, vol. 6, pp. 596-604.

Spuckler, C. M.; Siegel, R. (1994): Refractive index and scattering effects on radiation in a semitransparent laminated layer. *J. Thermopysics Heat Transfer*, vol. 8, pp. 193-201.

Szmyd, J. S.; Jaszczur, M.; Ozoe H.; Kakimoto, K. (2000): Numerical analysis of buoyancy driven convection and radiation from the free surface of the fluid in a vertical cylinder. Proc. 3rd Europ. Thermal Sci. Conf. (Heidelberg, Sepot. 2000).

Takagi, K.; Fukazawa, T.; Ishii, M. (1976): Inversion of the direction of the solid-liquid interface on the Czochralski growth of GGG crystals. *J. Crystal Growth*, vol. 32, pp. 89-94.

Tsukada, T.; Imaishi, N.; Hozawa, M. (1988): Theoretical Study of the Flow and Temperature Fields in CZ Single Crystal Growth. *J. Chem. Eng Japan*, vol. 21, pp. 184-191.

Tsukada, T.; Hozawa, M; Imaishi, N. (1994): Global analysis of heat transfer in CZ crystal growth of oxide. *J. Chem. Eng. Jpn.*, vol. 27, pp. 25-31.

Tsukada, T.; Kakinoki, K.; Hozawa, M.; Imaishi, N. (1995): Effect of internal radiation within crystal and melt on Czochralski crystal growth of oxide. *Int. J. Heat Mass Transfer*, vol. 38, pp. 2707-2714.

Whiffin, P. A. C.; Bruton, T. M.; Brice, J. C. (1976): Simulated rotational instabilities in molten bismuth silicon oxide. *J. Crystal Growth*, vol. 32, pp. 205-210.

Xiao, Q.; Derby, J. J. (1993): The role of internal radiation and melt convection in Czochralski oxide-growth - deep interface, interface inversion and spiraling. *J. Crystal Growth*, vol. 128, pp.188-194.

Xiao, Q.; Derby, J. J. (1994): Heat transfer and interface inversion during the Czochralski growth of Yttrium-Aluminum-Garnet and Gadolinium-Gallium-Garnet. *J. Crystal Growth*, vol. 139, pp.147-157.

Yuferev, V. S.; Budenkova, O. N.; Vasiliev, M.G.; Rukolaine, S. A.; Shlegel, V. N.; Vasiliev Ya. V.; Zhmakin, A.I. (2003): Variations of solid-liquid interface in the BGO low thermal gradients Cz growth for diffuse and specular side surface. *J. Crystal Growth*, vol. 253, pp. 383-397.